Quantum spin Hall effect in α-Sn/CdTe(001) quantum-well structures

Sebastian Küfner,* Lars Matthes, and Friedhelm Bechstedt
Institut für Festkörpertheorie und -optik, Friedrich-Schiller-Universität and European Theoretical Spectroscopy Facility (ETSF), Max-Wien-Platz 1, 07743 Jena, Germany
(Received 21 September 2015; published 13 January 2016)

The electronic and topological properties of heterovalent and heterocrystalline α-Sn/CdTe(001) quantum wells (QWs) are studied in dependence on the thickness of α-Sn by means of *ab initio* calculations. We calculate the topological $\mathbb{Z}_2$ invariants of the respective bulk crystals, which identify α-Sn as strong three-dimensional (3D) topological insulators (TIs), whereas CdTe is a trivial insulator. We predict the existence of two-dimensional (2D) topological interface states between both materials and show that a topological phase transition from a trivial insulating phase into the quantum spin Hall (QSH) phase in the QW structures occurs at much higher thicknesses than in the HgTe case. The QSH effect is characterized by the localization, dispersion, and spin polarization of the topological interface states. We address the distinction of the 3D and 2D TI characters of the studied QW structures, which is inevitable for an understanding of the underlying quantum state of matter. The 3D TI nature is characterized by two-dimensional topological interface states, while the 2D phase exhibits one-dimensional edge states. The two different state characteristics are often intermixed in the discussion of the topology of 2D QW structures, especially, the comparison of *ab initio* calculations and experimental transport studies.

DOI: 10.1103/PhysRevB.93.045304

I. INTRODUCTION

Topological insulators are insulators in the bulk system but exhibit metallic edge states at their surfaces or interfaces with a trivial insulator [1–5]. These edge states have special electronic properties, which give rise to the quantum spin Hall (QSH) phase, a new quantum phase of matter [6–8]. They possess a linear **k** dispersion and form Dirac cones. Their spin polarization may lead to intrinsic spin currents in the absence of an external magnetic field, but driven by the internal spin-orbit coupling. These peculiarities [9–12] are expected to offer novel applications in quantum computing and spintronics [1,13,14].

The group-IV material α-Sn and the II-VI compound semiconductor HgTe are ideal candidates to be topological insulators (TIs), because of their inverted band structures. In contrast to other tetrahedrally coordinated semiconductors, they are zero-gap semiconductors, as the fourfold degenerated Γ_{8v} states are energetically equivalent to the Fermi level [15]. In addition, as a consequence of the relativistic mass-Darwin effect, the *s*-like Γ_{6c} levels are energetically lower than the *p*-like Γ_{8v} levels and, hence, the band ordering is inverted with respect to conventional semiconductors like CdTe [15,16]. A minor strain, e.g., induced by growth on nearly lattice-matched substrates such as CdTe or InSb, opens a small gap between the Γ_{8v} states, which makes the materials insulating. In addition, the spin-orbit splitting between the Γ_{8v} and the Γ_{7v} states is of the order of magnitude of 1 eV, which is larger than the negative $\Gamma_{6c} - \Gamma_{8v}$ gap, and hence gives rise to the existence of the edge states within the negative gap [17,18].

The topology of a crystalline material can be characterized by a $\mathbb{Z}_2$ invariant index, which equals 1 in the case of a topological insulator and zero for topologically trivial systems. Within simplified electronic structure models such as the $\mathbf{k} \cdot \mathbf{p}$ theory, strained α-Sn and HgTe have been predicted as topological insulators calculating the $\mathbb{Z}_2$ index by means of the eigenvalues of the parity operator using the occupied electronic states at the time-reversal invariant momenta (TRIM) of the Brillouin zone (BZ) as basis set [18]. However, the parity method requires inversion symmetry, and is therefore not applicable to the zinc-blende material HgTe despite the use of arguments based on adiabatic continuity [18]. Yu *et al.* [19] proposed a method to calculate $\mathbb{Z}_2$ invariants, which does not require inversion symmetry and, importantly, is independent of a gauge fixing of the wave functions, which is critical in the case of *ab initio* calculations, because of the arbitrary phase factors of different wave functions at different **k** points. Such a self-consistent electronic-structure method has been applied to HgTe [19], but not to α-Sn.

In 2006, Bernevig *et al.* [10] predicted thick HgTe quantum wells (QWs) to be two-dimensional (2D) TIs. The QW structures consist of a HgTe film with thickness d_1 sandwiched between barrier layers of CdTe. The barrier material CdTe induces a confinement of electrons and holes in the HgTe layers in-between. For small layers of HgTe, the band ordering of the QW structure is that of a trivial insulator. With increasing HgTe thickness, however, the HgTe films dominate the electronic behavior of the QW. This effect is characterized by an inversion of the energetic ordering of the *s*- and *p*-like states in the center of the BZ close to the Fermi level and leads to a nontrivial topology of the QW structures in total [10,17,20,21]. In the inverted regime, the HgTe films begin to act like HgTe bulk and the situation becomes similar to that of two interfaces between two half-spaces of HgTe and CdTe, respectively. Due to the different electronic band structures of those materials, 2D topological interface states occur inside the interface planes between HgTe and CdTe, which has been recently demonstrated by *ab initio* calculations [17,20,21]. Despite the presence of these 2D topological interface states, the respective QSH phase can be made visible in experiments by one-dimensional (1D) topological edge states, which are characterized by a linear **k** dispersion in a 1D BZ and spin polarization such that electrons with opposite spin counterpropagate at the sample edges, if

*sebastian.kuefner@uni-jena.de

finite QW structures with surfaces perpendicular to the growth direction are investigated. In transport experiments, these 1D edge states are detected at the edges of 2D Hall bars made from finite QWs [11,22]. While the underlying physical reason in both cases is the nontrivial topology of the QW, it is important to point out, that two fundamentally different electronic states are concerned. This is especially important, as the 2D interface states, which are typically investigated by means of supercell calculations [17,20,21], have been mistakenly interpreted as the 1D edge states found in transport measurements [11,22] while actually being an indirect verification.

Because of the similarity of the bulk electronic structures and topology, basically the same effects as in the case of HgTe/CdTe QW structures should be expected for α-Sn/CdTe QWs. However, recent *ab initio* calculations showed [20] that α-Sn/CdTe(110) QWs do not exhibit a transition into the QSH regime because of strong interface dipoles induced by interface bonds due to the pronounced interface bond differences between α-Sn and CdTe compared to HgTe and CdTe. The accompanying strong electric fields in [001] direction arising from the interface electrostatics can be avoided, if the [001] growth direction is investigated instead of the [110] cleavage face of zinc-blende materials. The reason is that in [001] direction the atomic layers consist of the same atoms, alternating between anion and cation layers. Therefore, no in-plane dipole perpendicular to the growth direction can destroy the occurrence of the QSH phase. However, the stacking of differently charged layers raises another problem; a sawtooth potential inside the α-Sn QWs and CdTe barriers in growth direction created by differently charged α- Sn/Te and α-Sn/Cd interfaces at both interfaces [17]. No respective theoretical or experimental studies are yet available. How these effects influence the presence or absence of the QSH phase in α-Sn/CdTe(001) QWs is an open question.

In this paper, we study electronic and topological properties of α-Sn/CdTe(001) QWs by means of *ab initio* calculations. In Sec. II, the theoretical background, the numerical implementation and the studied structures are introduced. The results are presented in Sec. III. In a first step, in Sec. III A, the topological $\mathbb{Z}_2$ invariants are calculated, whereby the 3D TI character of α-Sn and the trivial character of CdTe is proven. In the subsequent Sec. III B, interface electrostatics and band offsets of α-Sn/CdTe(001) QW structures depending on the thicknesses of both materials are discussed. The resulting types of the heterostructures are identified and possible effects on the electronic structure of the respective interfaces are investigated. In the following part, in Secs. III C 1 and III C 2, the electronic structure depending on the QW thickness of these QW structures is described. It is shown, that a phase transition occurs from a topologically trivial insulating phase into a QSH phase, which is characterized by two-dimensional topological states. The characteristic thickness of α-Sn, where this transition occurs, is calculated and the 2D topological interface states are characterized in detail concerning their localization, spin polarization, and band dispersion. In a final step, in Sec. III D, we address the issue of the distinction of these interface states from the topological 1D topological edge states, which should be visible in transport experiments.

II. THEORETICAL AND COMPUTATIONAL METHODS

A. Total energy calculations and atomic models

We apply the density functional theory (DFT) [23] within the local density approximation (LDA) [24] as implemented in the Vienna *ab initio* Simulation package (VASP) [25,26]. Exchange and correlation (XC) are treated using the Monte Carlo simulation results of Ceperly and Alder [27] as parametrized by Perdew and Zunger [28]. The scalar-relativistic effects and spin-orbit coupling [29] are included in the electronic-structure calculations. To describe the electron-ion interaction, pseudopotentials are used, which are generated within the projector-augmented wave (PAW) [30,31] method. The Sn $5s$, Sn $5p$, Cd $4d$, Cd $5s$, Te $5s$, and Te $5p$ electrons are explicitly treated as valence electrons. Outside the PAW spheres, the single-particle Kohn-Sham wave functions are expanded into a plane-wave basis set. We apply a plane-wave energy cutoff of 500 eV for bulk calculations or 275 eV for the superlattices. Bulk BZ integrations are replaced by a sum over $12 \times 12 \times 12$ Monkhorst-Pack [32] $\mathbf{k}$ points. For the superlattice calculations, a BZ sampling of $6 \times 6 \times 1$ Monkhorst-Pack $\mathbf{k}$ points is used. We found the optimized lattice constants of the bulk materials to be $a_0 = 6.475$ Å (α-Sn) and $a_0 = 6.46$ (CdTe). The calculated lattice constant of α-Sn is in agreement with the values measured by Farrow [33] and Davey [34] using x-ray diffraction. A slight underestimation of 5 mÅ (Ref. [33]) and 15 mÅ (Ref. [34]), respectively, within DFT-LDA can be explained by the well-known tendency of the LDA to underestimate bond lengths [35]. The optimized lattice constants of CdTe slightly deviate from the experimental value of $a_0 = 6.48$ Å (CdTe) [36] because of the used XC potential. However, in another data collection a measured value of $a_0 = 6.460$ Å [37] (CdTe), which is much closer to the theoretical lattice constant, has been published.

Local or semilocal XC potentials significantly underestimate fundamental energy gaps [38]. In addition, in the case of the zero-gap semiconductor α-Sn, an artificial metallic behavior is obtained because of a negative indirect $\Gamma - L$ gap. Moreover, within these approximations, the energetic order of the Γ_{7v} and Γ_{6c} levels is interchanged [39]. For bulk calculations, these problems can be overcome applying the HSE06 hybrid functional [40], which includes a screened nonlocal exact Fock exchange, although computed using the Kohn-Sham single-particle wave functions. Unfortunately, this method is computationally too expensive to be applied in the case of nanostructures such as multi-QW structures. Therefore, we apply the Tran-Blaha method (MBJLDA) with the modified Becke-Johnson (MBJ) semilocal exchange functional [41] in the case of superlattice calculations, in order to approximate the quasiparticle effects beyond the LDA level. It is based on a model exchange potential designed to reproduce the shape of exact-exchange optimized effective potentials [42] and its reliability has been demonstrated for many zinc-blende compounds [43,44]. We find reasonable agreement of the electronic structure results computed within MBJLDA compared to experimental findings and HSE06 calculations [17]. Usually, the application of the MBJLDA is restricted to homogeneous systems because it involves a material-specific parameter CMBJ. However, we find a joint parameter CMBJ $= 1.235$ to describe both materials, α-Sn and

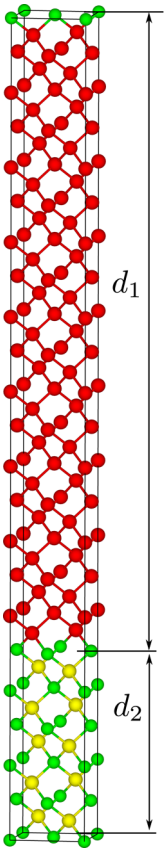

FIG. 1. Symmetric unit cell of a $(\alpha\text{-Sn})_{33}(\text{CdTe})_5(\text{Te})_1(001)$ superlattice. The Sn (Cd,Te) atoms are shown as red (yellow, and green, respectively) dots.

CdTe, with reasonable accuracy. This allows the application of the MBJLDA to α-Sn/CdTe heterostructures.

An α-Sn/CdTe(001) multi-QW structure with an α-Sn film thickness d_1 could be modeled by a corresponding superlattice with a sufficient thickness d_2 of the CdTe barrier layers. However, $(\alpha\text{-Sn})_N(\text{CdTe})_M(001)$ superlattices with N α-Sn atomic layers and the corresponding number M of neutral bilayers of CdTe consist of inequivalent Sn-Cd and Sn-Te interface bonds and, hence, give rise to interface dipoles in normal direction. To obtain equivalent bonds between the two materials, i.e., the same termination of the CdTe barriers at the two interfaces in the supercells, e.g., the Te termination, nonstoichiometric CdTe barriers must be used. In the actual calculations, we add to the M CdTe(001) bilayers an additional Te monatomic layer. It makes the barriers nonstoichiometric with $(\text{Te})_1(\text{CdTe})_M \triangleq \text{Cd}_M\text{Te}_{M+1}$. In order to allow for a translationally invariant bond stacking, an odd number N of atomic Sn layers is applied resulting in $(\alpha - \text{Sn})_N(\text{Te})_1(\text{CdTe})_M$ unit cells as illustrated in Fig. 1 with $N = 33$ and $M = 5$. Thereby, we request N to be an odd number, whereas $N + 2M + 1$ should be mod 4 because an irreducible (001) slab of the zinc-blende crystal consists of four atomic layers [45]. These unit cells are symmetric with the consequence that no net dipoles and sawtooth potentials in growth direction can appear. The bulk lattice constants of CdTe and α-Sn slightly differ by 0.23%. To adapt this lattice mismatch, we assume that only the α-Sn layers are strained [46]. The in-plane lattice constants are fixed in accordance to the calculated lattice constant of CdTe. Using the ratio of the elastic constants of α-Sn the biaxial coefficient $R_b = -\frac{2C_{12}}{C_{11}} = -0.85$ [47] determines the distances between layers in [001] direction. As an example, the unit cell of an $(\alpha - \text{Sn})_{33}(\text{Te})_1(\text{CdTe})_5(001)$ superlattice is displayed in Fig. 1. Since generally the superlattice constant in [001] direction is large enough to avoid the wave-vector dispersion in this direction, we discuss the resulting electronic properties in the translational symmetry perpendicular to the [001] axis. They are presented versus the 2D square BZ whose extent is given by the lateral lattice constant of the superlattice, i.e., of CdTe.

B. Numerical calculation of topological invariants

The topology of the band structure of an insulating bulk system can be characterized by $\mathbb{Z}_2$ topological invariants [5,9,18,48]. For diamond and zinc-blende crystals there are four $\mathbb{Z}_2 = (\nu_0; \nu_1, \nu_2, \nu_3)$ invariants, that allow one to distinguish three categories of materials: ordinary insulators, strong TIs, and weak TIs (in three dimensions). The strong TIs are characterized by $\nu_0 = 1$ allowing for the existence of topologically protected, spin-polarized surface or edge states, and hence the QSH phase [1,5,8,18]. ν_0 is called the strong $\mathbb{Z}_2$ invariant because it distinguishes the strong TIs from the weak TIs. The weak TIs refer to $\nu_0 = 0$, while some or all of the $\nu_k, k \in \{1,2,3\}$ equal 1. However, topologically nontrivial ν_k also exhibit chiral edge states, but they depend on the choice of the lattice vectors and are not preserved in the presence of weak disorder [8,18]. The weak $\mathbb{Z}_2$ numbers are nonetheless important when clean surfaces are studied. In the case of trivial insulators, all four $\mathbb{Z}_2$ invariants are zero, and no chiral edge states occur.

For systems with inversion symmetry such as diamond α-Sn, the four invariants can be determined from the parity of the occupied Bloch states at the TRIM points of the BZ [18]. They follow from the evaluation of the matrix elements of the parity operator. Because of the inversion symmetry this method can be applied. The biaxial strain leads to a tetragonal symmetry of the α-Sn layers, the fourfold degeneracy of the Γ_{8v} level is lifted, and the α-Sn films become insulators. The symmetry labels of the unstrained diamond lattice symmetry do not, in principle, apply for the resulting tetragonal structures. Nevertheless, the $\mathbb{Z}_2$ class of strained HgTe and α-Sn have been determined applying the ideal diamond lattice with inversion symmetry based on arguments of adiabatic continuity [18].

Another possibility proposed by Fu and Kane [18,48] is the determination of the $\mathbb{Z}_2$ invariants from the Pfaffian of the matrix elements of the time-reversal operator using the occupied band states at TRIM points as basis set. Despite the fact that the resulting $\mathbb{Z}_2$ invariants calculated by means of the Pfaffian matrix method are gauge independent, the method itself depends on a gauge transformation [18,48]. However, using *ab initio* methods, the electronic wave functions of different band states and at different **k** points do not have a fixed phase relation to each other but random phase factors. This makes a gauge fixing of the wave functions obtained from *ab initio* calculations nontrivial [19,49–51]. Both methods to evaluate the topological class from the parities of the occupied

bands as well as the Pfaffian matrix method are consequently not appropriate to calculate the $\mathbb{Z}_2$ class of materials lacking inversion symmetry and using *ab initio* methods.

In 2011, Yu *et al.* [19] proposed an expression of the $\mathbb{Z}_2$ invariant of bulk insulators using the non-Abelian Berry connection. We use this method to compute the $\mathbb{Z}_2$ invariants, and implement it in the VASP code. It does not require gauge fixing of the wave functions or inversion symmetry and can therefore be directly applied to *ab initio* calculated wave functions.

According to the Fu-Kane theory, the number of Kramers pair switchings modulo 2 along a line connecting two time-reversal invariant momenta is equivalent to the topological invariant of the system [5,8,18,48]. Yu *et al.* [19] showed that in the two-dimensional case, the Kramers pair switching is equivalent to the "partner switchings" of the Wannier function centers (WCCs) during a closed loop in the Brillouin zone. The starting point for the actual calculation is, that the evolution of the Wannier charge centers can be related to the phase of the eigenvalues of the position operator $\mathbf{x}$ projected onto the occupied band states. This eigenvalue problem of the position operator is then solved by a transfer integral method.

In a first step, the calculation of the $\mathbb{Z}_2$ invariant of two-dimensional systems is explained. The treatment of three-dimensional systems can then be extended to its two-dimensional subsystems. A two-dimensional Brillouin zone spanned by the two reciprocal lattice vectors $\mathbf{b}_x$ and $\mathbf{b}_y$, which are not required to be orthogonal to each other, is considered. The Brillouin zone is discretized in $N_x \times N_y$ intervals with the interval lengths $\Delta k_{x,y} = \frac{2\pi}{N_{x,y}a}$, where $\frac{\pi}{a}$ is the distance between Γ and the BZ boundary. In order to keep the notation consistent with the literature [19,51], the values of the k_j are from now on given in units of $\frac{1}{a}$. This means, that the k_j ($j = x,y$) run from 0 to π for a full path through the BZ parallel to $\mathbf{b}_j$. We calculate the overlap matrices between the Bloch periodic parts $|n,k_x,k_y\rangle$ of the occupied wave functions along lines parallel to $\mathbf{b}_x$ with fixed k_y:

$$(F_{i,i+1}(k_x,k_y))^{m,n} = \langle m,i\Delta_{k_x},k_y|n,(i+1)\Delta_{k_x},k_y\rangle. \quad (1)$$

Here, n and m denote the band indices and run over the $2N$ occupied bands, where the factor 2 represents the Kramers degeneracy, and $i = 0 \ldots N_x$ defines the position in the discretized BZ. Consequently, the resulting $\hat{F}(k_x,k_y)$ is a $2N \times 2N$ matrix. The overlap integrals fix the phase between adjacent Bloch states even in the absence of gauge invariance.

In a next step, the $2N \times 2N$ matrix $\hat{D}(k_y)$ is calculated as the matrix product of all $F_{i,i+1}(k_x,k_y)$ along a line parallel to $\mathbf{b}_x$:

$$\hat{D}(k_y) = \hat{F}_{0,1}\hat{F}_{1,2}\hat{F}_{2,3}\cdots\hat{F}_{N_x-2,N_x-1}\hat{F}_{N_x-1,0}. \quad (2)$$

The last multiplication with $F_{N_x-1,0}$ is critical for the purpose of gauge fixing, because it connects the last point of each path parallel to $\mathbf{b}_x$ with the respective starting point yielding a closed loop in $\mathbf{k}$ space. The matrix $\hat{D}(k_y)$ is diagonalized yielding $m = 1 \ldots 2N$ complex eigenvalues $\lambda_m(k_y) = |\lambda_m(k_y)|e^{i\theta_m(k_y)}$. Their phases $\theta_m(k_y)$ are identified with the position of the Wannier charge centers and invariant under a $U(2N)$ unitary transformation of the occupied band states. Therefore, the arbitrary phase factors resulting from the independent calculation of different wave functions at different $\mathbf{k}$ points within *ab initio* calculations are eliminated.

The topological invariant of the system is calculated by the number of crossings of an arbitrary horizontal reference line connecting two TRIM points with k_y running from zero to π with the Wannier center evolution curves $\theta_m(k_y)$ mod 2.

For three-dimensional systems it is possible to derive all four $\mathbb{Z}_2$ invariants dividing them in two-dimensional subsystems [19,49]. We consider six 2D subsystems in reciprocal space defined by one of the momenta fixed at $k_j = 0$ and $k_j = \pi$ with $j \in \{x,y,z\}$, each containing four TRIM points. The weak topological indices $\nu_k = (\nu_1,\nu_2,\nu_3)$ are identified with the $\mathbb{Z}_2$ indices of the planes $k_j = \pi$. They obviously depend on the choice of the reciprocal lattice vectors and hence are not protected against weak disorder. The strong $\mathbb{Z}_2$ index ν_0 is equivalent to the sum of the $\mathbb{Z}_2$ invariants of two "opposite" $k_j = 0$ and $k_j = \pi$ planes mod 2 for each of the three pairs given by $j = 1,2,3$. A strong TI therefore requires that for each pair of 2D subsystems the respective $k_j = 0$ and $k_j = \pi$ planes have different $\mathbb{Z}_2$ invariants. However, there is some redundancy involved in the choice of the actual planes used for the calculation of ν_0 as each of the three pairs in $j = 1,2,3$ gives the same result [49]. The strong $\mathbb{Z}_2$ index is therefore obviously independent of the choice of the reciprocal lattice vectors.

III. RESULTS AND DISCUSSION

A. $\mathbb{Z}_2$ invariants

The resulting WCC evolution curves of slightly biaxially strained α-Sn and CdTe are shown in Fig. 2. In the cases of α-Sn it is clearly visible that the $k_z = 0$ related 2D subsystem exhibits a topologically nontrivial behavior with $\mathbb{Z}_2 = 1$. The reference lines are crossed by an odd number of WCC evolution curves indicating an odd number of Kramers pair switchings. The opposite face in the BZ $k_z = \pi$, in contrast, shows no crossing or an even number of crossings with a reference line and the WCC evolution curves resulting in $\mathbb{Z}_2 = 0$. From the different topological indices of the two 2D subsystems, it follows that the strong $\mathbb{Z}_2$ index of the three-dimensional system ν_0 equals 1, identifying strained α-Sn as a strong topological insulator. We also calculated the weak topological indices, which are identical with the $\mathbb{Z}_2$ index of the three faces belonging to $k_j = \pi$, which equal zero for all $j \in \{x,y,z\}$. The resulting $\mathbb{Z}_2$ class of biaxially strained α-Sn is $(1;0,0,0)$, in accordance with predictions based on parity evaluation for diamond α-Sn combined with arguments based on adiabatic continuity [18].

Interestingly, test calculations performed with the ideal unstrained structures also identify α-Sn as a strong topological insulator with $\nu_0 = 1$. This is astonishing as it contradicts somehow the original definition of a topological insulator, which requires an insulating bulk system [18], in whose fundamental gap the metallic topological states may appear. Here, the strain and therefore the splitting of the Γ_{8v} states may be infinitely small. The driving factor for the strong TI character of both materials might be the band inversion with occupied Γ_{6c} and two empty Γ_{8v} states. This is in accordance with first-principles surface calculations that show the existence of topological surface states at α-Sn(001) surfaces regardless of the absence of strain [52].

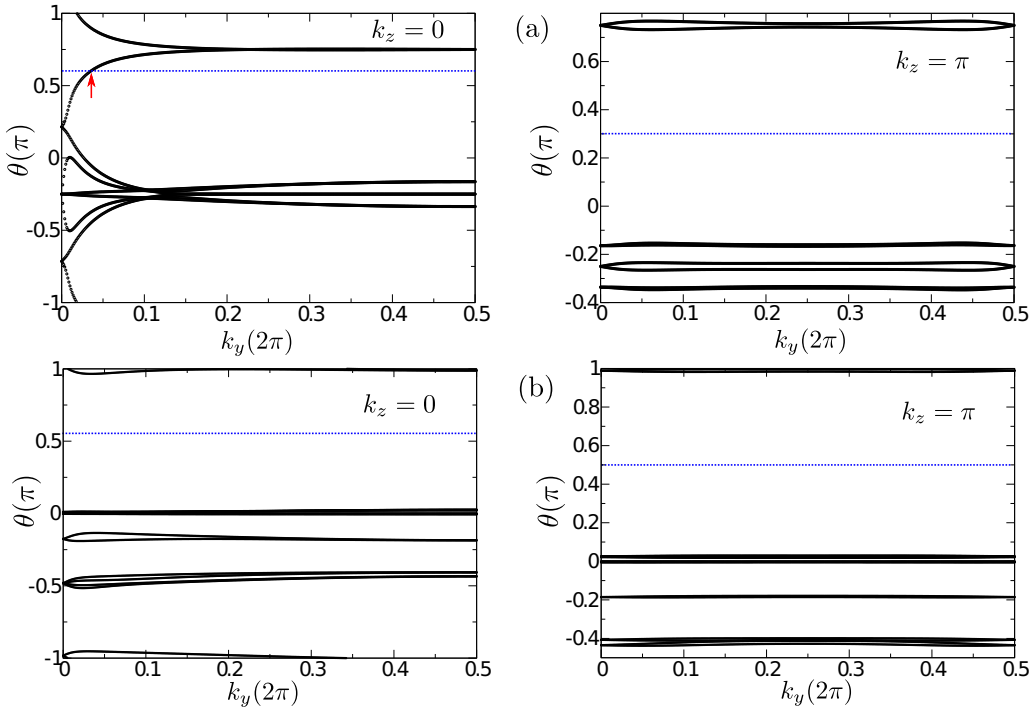

FIG. 2. WCC evolution curves of 0.15% biaxially strained α-Sn (a) and CdTe (b) in the 2D subsystems defined by $k_z = 0$ and $k_z = \pi$ of the zinc-blende lattice. Possible reference lines are depicted in blue. Red arrows indicate the crossing points of the WCC curves and the reference lines.

The WCC evolution curves along k_y for $k_z = 0$ and $k_z = \pi$ of CdTe are depicted in Fig. 2(b). The other faces are not shown, because they are topologically equivalent to the latter ones. All 2D subsystems are characterized by a trivial $\mathbb{Z}_2$ index, as the reference lines do not or twice cross the WCC evolution curves. Consequently, CdTe and can be identified as topologically trivial insulators with the $\mathbb{Z}_2$ class $(0;0,0,0)$.

The different $\mathbb{Z}_2$ classes of α-Sn and CdTe suggest the occurrence of the QSH phase in the α-Sn QWs due to the boundaries between both materials, which will be discussed in detail in the following sections.

B. Band offsets and confinement of electron and hole states

In the present section, the valence band offset $\Delta E_v = \varepsilon(\Gamma_{8v},\alpha\text{-Sn}) - \varepsilon(\Gamma_{8v},\text{CdTe})$ between the Γ_{8v} levels in α-Sn and and CdTe are investigated in order to obtain information about the quantum confinement of electron and hole states in the QW structures and their dependence on the thicknesses of both material layers.

In a first approach, we calculate the natural band discontinuity between α-Sn and CdTe by means of the alignment of the two bulk band structures using their branch points, or charge neutrality levels, E_B [53,54]. We apply the method of Schleife *et al.* [55] together with band structure calculations based on the hybrid HSE06 XC functional. We find $E_B = 0.71$ eV (CdTe) and -0.52 eV (α-Sn) with respect to the Γ_{8v} valence band top. The value for CdTe is in good agreement with results of earlier computations [53]. Therefore, at α-Sn/CdTe interfaces, a natural valence band discontinuity of $\Delta E_v = 1.26$ eV is predicted, which is in good agreement with the measured value of $\Delta E_v = 1.1$ eV [56]. Consequently, the Γ_{8v} level of α-Sn is only about 300 meV lower in energy than the Γ_{6v}-derived conduction band edge of CdTe and strong confinement of holes is expected. The confinement of electrons is, however, more difficult to evaluate because of the inverted α-Sn bulk band structure.

However, the model of "natural band discontinuities" neglects real-structure effects at the interfaces. The influences of the atomic interface structure, the interface electrostatics, and confinement effects in quantum well structures are neglected within the branch point method [57,58]. These effects can be included in the calculation of the valence band offsets, if the electrostatic potential in combination with a self-consistent interface calculation is used for an alignment of the band structures [57,58]. This method has been described in detail elsewhere [17]. Here, we take such effects into account because of the use of atomic models for the interfaces as illustrated in Fig. 1.

Following this approach, in α-Sn/CdTe QWs with (001) orientation we find the fundamental gap of the QW structures to be completely inside the projected valence bands of CdTe, which seems to be obviously unphysical. However, as will be discussed in the next section, Sec. III C, the required thicknesses of the α-Sn layer are of the order of magnitude of 10 nm, which inevitably limits the barrier thickness of CdTe to 9.6 Å for reasons of computational cost. In addition, as explained in Sec. II A, due to the structure of the CdTe barrier consisting of polar layers in (001) direction, nonstoichiometric barriers must be used to avoid an intrinsic electrostatic sawtooth potential. The small barrier thickness together with the violated stoichiometry may be the reason for a surprising band alignment. This is verified by the comparison of the plane-averaged electrostatic potentials of QWs containing 33

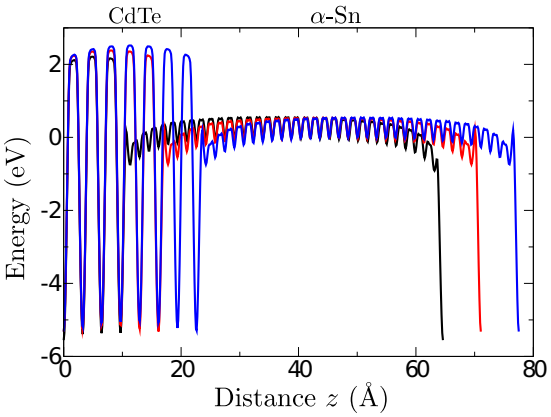

FIG. 3. Plane-averaged electrostatic potential $V_{es}(z)$ of $(\alpha\text{-Sn})_{33}(\text{Te})_1(\text{CdTe})_3(001)$ (black line), $(\alpha\text{-Sn})_{33}(\text{Te})_1(\text{CdTe})_5(001)$ (red line), and $(\alpha\text{-Sn})_{33}(\text{Te})_1(\text{CdTe})_7(001)$ (blue line) QWs. The space-averaged electrostatic potential of the superlattice is used as absolute energy zero.

atomic layers of α-Sn but increasing CdTe barrier thicknesses of 9.6, 16.1, and 22.5 Å in Fig. 3. It is obvious that the electrostatic potential in the α-Sn region 10 Å away from the interface is well converged, as the atomic oscillations are equally high. In the CdTe barriers of the QW, there is a small upward shift of the atomic oscillations with increasing barrier thickness. The difference between the smallest barrier and the largest one amounts to roughly 300 meV. This upward shift of the energy scale of the superlattice with respect to that of CdTe bulk causes the conduction band minimum of bulk CdTe to be just above the conduction band minimum of the respective supercells. However, the envelope of the maxima of the atomic oscillations of the electrostatic potential is not flat in the whole barrier region, even in the case of the largest barrier considered here, indicating that the potential is not yet completely converged and a further thickness increase would therefore lead to a further decrease of the valence band discontinuity. The valence band discontinuity is found to be rather independent of the thickness of the α-Sn film. Consequently, the situation with the fundamental gap being inside the projected bulk gap of CdTe, which is found for the 22.5-Å-wide CdTe barrier, will be considered in the discussion of the electronic band structure, despite the fact that in the actual calculations smaller CdTe barriers are used.

C. Quantum-well band structures and topological states

The nontrivial topology of α-Sn triggers the expectation of the existence of a 2D quantum spin Hall phase characterized by metallic, linearly dispersed, helical edge states in the interface plane to a trivial insulator like CdTe following the definition of a 3D topological insulator. However, in a superlattice the situation is different to that of an isolated interface between two half-spaces due to confinement effects. Only for sufficiently large thicknesses of the α-Sn and CdTe films can it be expected that the multi-QW structure behaves like a series of interfaces and hence exhibits the 2D QSH effect in the α-Sn layers, which, importantly, in this case is a result of the 3D TI nature of α-Sn. The existence of this effect depends on the thickness of the α-Sn content.

1. Quantum spin Hall effect

The quasiparticle subband structures of the $(\alpha - \text{Sn})_N\text{Te}_1(\text{CdTe})_{10}(001)$ QW structures with varying well

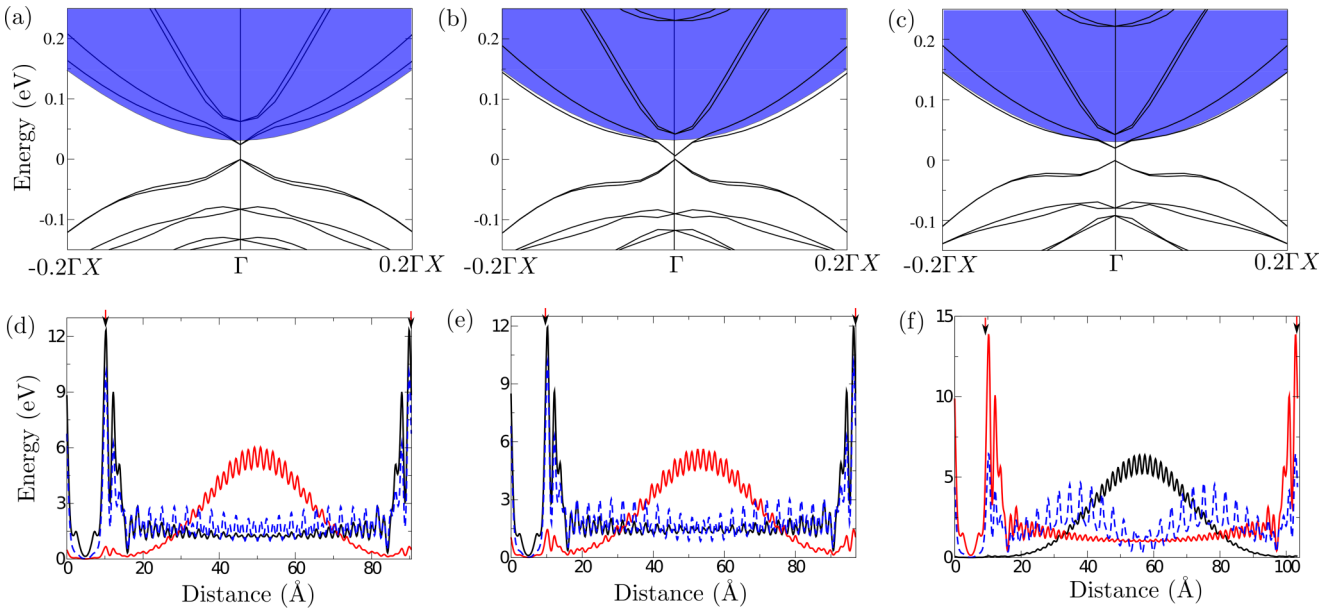

FIG. 4. Subband structures of $(\alpha\text{-Sn})_N(\text{Te})_1(\text{CdTe})_5(001)$ superlattices for different QW thicknesses $N = 49$ (a) and (d), $N = 53$ (b) and (e), and $N = 57$ (c) and (f). The blue background indicates the projected bulk band structure of the CdTe barrier material. The energy of the highest occupied SL state is used as energy zero. In the lower panels, the wave-function squares of the lowest unoccupied (black), the highest occupied (red), and the second-highest occupied (blue) states at Γ, averaged over planes perpendicular to the QW orientation [001], as a function of the distance z for the respective SLs with $d_1 = 8.1$ nm (a) and (d), 8.8 nm (b) and (e), and 9.4 nm (c) and (f). Red arrows indicate the position of the interfaces.

thicknesses $N = 49$, 53, and 57 are depicted in Figs. 4(a)–4(c) in the vicinity of the Γ point of the 2D BZ of the interface [45] in the direction $\pm\Gamma X \parallel [\pm 100]$. All these heterostructures exhibit an insulating band structure. The fundamental gap at Γ is, however, almost closed for the superlattice (SL) with $N = 53$. It is clearly visible, that the highest occupied as well as the lowest unoccupied SL state exhibit a linear dispersion in the vicinity around the Γ point implying the formation of Dirac cones. This behavior is less pronounced in the cases $N = 49$ and 57, where the linear conduction band states also penetrate deeper into the projected bulk band gap of CdTe than for the superlattice with $N = 49$. The formation of 2D Dirac cones is an indication for a topological transition from a trivial insulating phase into the quantum spin Hall phase for increasing α-Sn thickness. The existence of Dirac cones is not, however, sufficient to claim the existence of a quantum spin Hall phase. The edge character in terms of a localization at the interface between α-Sn, the characteristic spin polarization, and the topological protection remain to be shown. We will address these issues in the following.

In order to investigate the localization behavior of the subband states near Γ around the Dirac point, Figs. 4(d)–4(f) show the wave-function squares of the states closest to the Fermi energy along the interface normal direction. The variation of the maxima of the atomic oscillation can be interpreted as the envelope function of the respective subband state.

In the case of the smallest QW [see Fig. 4(d)], the probability density of the lowest unoccupied state is localized inside the interface plane and decays exponentially into the α-Sn film, whereas the probability density almost vanishes inside the confining CdTe barrier regions. In combination with the linear dispersion, this is a clear indication for the beginning of edge state formation. The envelope function of the highest occupied state clearly exhibits the shape of an $n = 1$ confined state in a rectangular quantum well. It is located inside the α-Sn region with one pronounced maximum and an almost vanishing probability density inside the CdTe layer. The second highest unoccupied state in the α-Sn QW has an elevated probability density at the edges very similar to the lowest unoccupied one. However, there are two much smaller maxima inside the α-Sn layer, and it might be an $n = 2$ confined QW state.

For the $N = 53$ QW, which exhibits the typical Dirac-cone dispersion [see Fig. 4(e)] with vanishing gap, the localization properties do not change significantly. The highest occupied state is found to be an $n = 1$ confined state. The second highest occupied state as well as the lowest unoccupied states are located at the interface and decay exponentially inside the α-Sn region, whereas the probability density is close to zero in the CdTe barriers. This behavior is typical for topological edge states, if their helical spin character can be proven (see below).

For the largest QWs studied, the corresponding wave functions are depicted in Fig. 4(f). There is a significant change in the localization properties of the states close to the Fermi energy. The envelope function of the highest occupied and the lowest unoccupied state are interchanged with respect to the situation shown in Fig. 4(e), while the localization of the second highest occupied state remains unchanged. This interchange is remarkable, as it indicates an interchange in the band ordering and, therefore, might change the topological invariant of the whole quantum well. This issue will be addressed including an analysis of the atomic orbital character of the corresponding subband states in Sec. III D. It can be concluded, that the increase of the α-Sn film thickness and the formation of the Dirac cones is accompanied by a significant change of the localization character of the states closest to the Fermi level. For a definite proof of the topological origin of the linear edge states, their spin polarization has still to be proven.

2. *Spin polarization of interface states*

The local magnetization densities at Γ for the QW structure with $d_1 = 8.8$ nm (α-Sn) are depicted in Fig. 5 for the highest

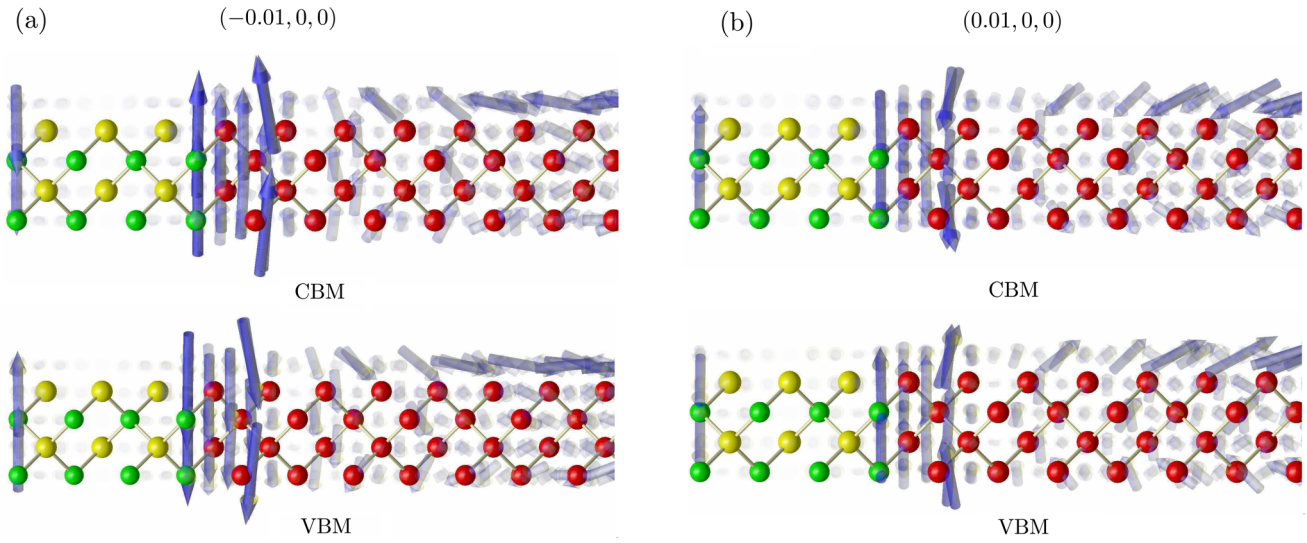

FIG. 5. Local magnetization of the lowest unoccupied state (a), and the highest occupied state (b) in the vicinity of the Γ point in $\pm\Gamma X$ direction of a $(\alpha\text{-Sn})_{53}(\text{Te})_1(\text{CdTe})_5(001)$ QW in the region of the interface. A view from [010] is depicted. The points (±0.01,0,0) mark the location of the considered state in **k** space in units of the reciprocal lattice.

occupied and lowest unoccupied subbands in the vicinity of the Γ point in $\pm\Gamma X$ direction near one interface. For both, the highest occupied as well as the lowest unoccupied subband, the spin polarization is mainly perpendicular to the interface normal and shows a rotation of π between the $-X \rightarrow \Gamma$ and the $\Gamma \rightarrow X$ direction. This spin flip for a switch from the direction $\mathbf{k}$ to $-\mathbf{k}$ in the 2D BZ is a consequence of the time-reversal symmetry. This spin polarization is characteristic for topological edge states. In combination with the linear dispersion of the Dirac cones in Fig. 4(b) and the localization at the interface in Fig. 4(e), this is a clear indication of the presence of the quantum spin Hall effect.

The topological protection of those states, i.e., their robustness against changes in the interface orientation, is however difficult to prove. Recent *ab initio* investigations [21] of α-Sn/CdTe(110) QWs revealed that in these structures an intrinsic electric field caused by the atomic geometry and bonding in the interface inhibits the occurrence of the QSH phase. Nevertheless, topological surface states (TSSs) at the α-Sn(001) surface have been demonstrated by means of *ab initio* calculations [52] and angle-resolved photoemission spectroscopy (ARPES) [59,60]. In the case of the α-Sn/CdTe interface as well as for the α-Sn surface, the physical reason for the occurrence of the topological states is the same. The topological states occur at the spatial interface between the topologically nontrival α-Sn and a topologically trivial region, i.e., CdTe (in the case of the α-Sn/CdTe interface with thick enough α-Sn films) and the vacuum (for the α-Sn surface), respectively. Therefore, the existence of the TSSs in α-Sn(001) surfaces with a totally different passivation as in the interface case might be considered as an additional indication of the topological protection of those states.

D. Dimensionality of topological states

The switch in the localization behavior between the highest occupied and the lowest unoccupied state, as discussed in Sec. III C 1, is a first indication of a level inversion and a possible resulting change in the topology of the quantum-well system versus thickness. In order to allow for an even more detailed analysis of the band order inversion, the projections of the band states onto atomic *s* and *p* orbitals are shown in Fig. 6 depending on the QW thickness for a much larger range of the α-Sn content than which has been discussed so far, in particular, in Fig. 4.

For $N < 53$, the orbital-symmetry projections in Fig. 6(a) show that the lowest unoccupied level is mainly formed by *s* orbitals, whereas in the subband below the Fermi level at Γ [Fig. 6(b)] the projections onto *p* orbitals dominate. The QWs with thicknesses below $d_1 \lesssim 8.1$ nm are trivial insulators with a band ordering (at least with respect to the orbital symmetries) similar to that of CdTe. For thicknesses larger or equal to $N = 57$, this energetic level ordering is inverted similar to the bulk band structure of α-Sn. The corresponding topological transition, where the level ordering of *s*- and *p*-like states is inverted, is found to occur between $d_1 = 8.1$ nm and $d_1 = 9.4$ nm. However, test calculations also show a weak dependence of the critical thickness of the α-Sn film, where the level inversion takes place, on the CdTe barrier thickness. This fact is probably a consequence of the CdTe thickness-dependent band discontinuities and the resulting confinement situations (see Sec. III B). From Fig. 6(c), it is obvious, that the second highest occupied subband is formed by atomic *p* orbitals, independently of the QW thickness, and its orbital symmetry remains, hence, uninfluenced by the topological transition. Unfortunately, neither theoretical nor experimental values for comparison of the critical thickness in α-Sn/CdTe QW structures have been published so far.

In the inverted regime, $d_1 \gtrsim 8.1$ nm, the studied α-Sn/CdTe QW structures have been identified as topological insulators. The appearing quantum spin Hall phase has been essentially characterized by the occurrence of two-dimensional topological interface states which are (i) localized at both α-Sn/CdTe interfaces of each quantum well, (ii) two-dimensional, i.e., dependent on the wave vector in the 2D BZ of the interface, and (iii) spin polarized. Since the α-Sn QW thickness is relatively large, the corresponding multi-QW structures may be interpreted as a 3D TI bulk material. The character of the topological interface states is similar to those discussed theoretically [52] and experimentally [59,60] for surfaces of α-Sn crystals. Since they are topologically protected, the chemical nature of the surface passivation, here due to the adjacent CdTe barrier material or Te layers, should not play a significant role. This situation is schematically depicted in Fig. 7(a). The 2D topological interface states have been characterized in Sec. III C. Similar results based on *ab initio* supercell calculations were previously reported for the case of HgTe/CdTe QW structures [17,20,21]. However, an experimental proof of these interface states, for example by means of ARPES, is very challenging because of the required

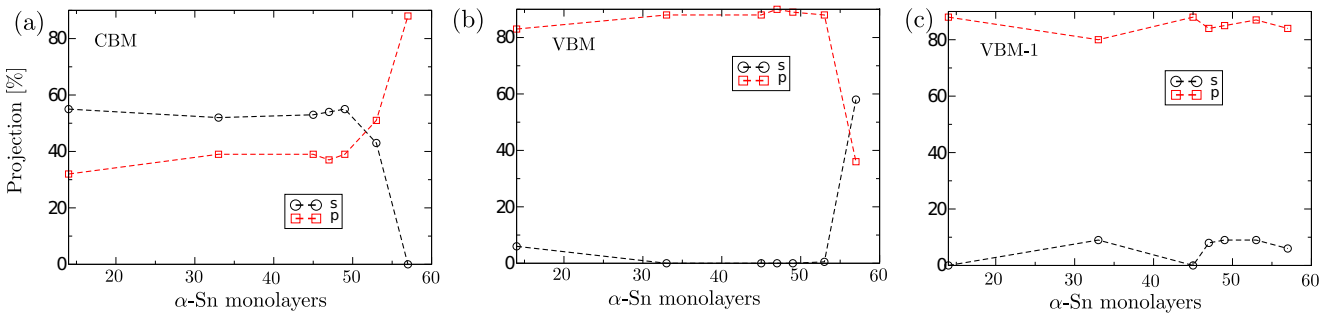

FIG. 6. Contributions of atomic *s* and *p* orbitals to the subband states close to the Fermi level of $(\alpha\text{-Sn})_N(\text{Te})_1(\text{CdTe})_5(001)$ superlattices depending on the QW size. In (a), the lowest unoccupied subband (CBM) is depicted, while (b) refers to the highest occupied subband (VBM), and (c) shows the second highest occupied subband (VBM-1).

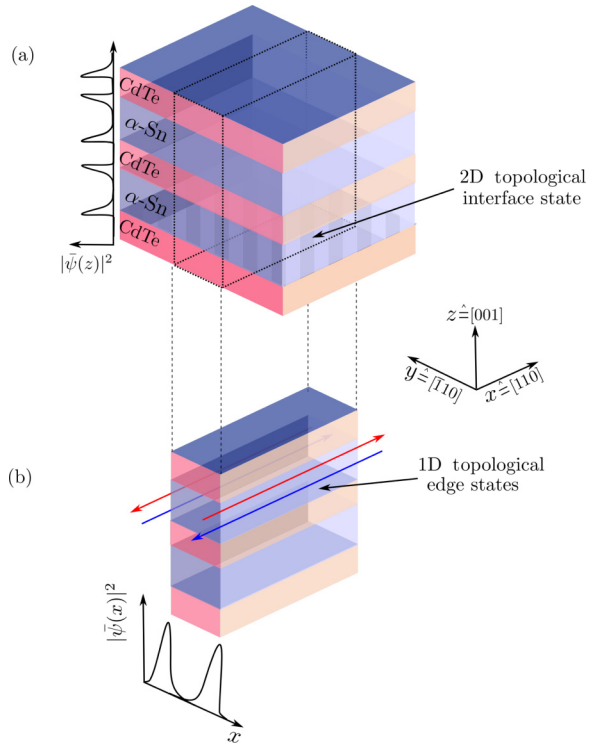

FIG. 7. Schematic representation of dimensionality and localization of the topological states in 3D multi-QW structures (a) and finite ones (b) produced as ribbons from the geometry in (a). In (a), one of the two-dimensional interface states located inside the interface planes between α-Sn and CdTe in a 3D α-Sn/CdTe(001) QW structure is highlighted exemplarily by hachures. In (b), the one-dimensional topological edge states at the edges of a 2D Hall bar made from a α-Sn/CdTe(001) QW structure are indicated. The spin polarization of the edge states is indicated by the color of the arrows. Red (blue) color may indicate spin-up (spin-down) electrons, which counterpropagate at a given edge. In both cases, the localization of the states is indicated by the schematic wave-function square depending on the plane-averaged (a), and line-averaged (b) topological states, respectively.

large escape depth of the electrons along the interface normal or the reduced barrier thickness.

A more direct or indirect way to detect indications for the QSH phase are transport measurements as demonstrated for HgTe/CdHgTe QW structures [11,22]. In these experiments, however, the dimensionality of the QW structure in the inverted regime is reduced toward a 2D Hall bar geometry. The resulting system has a reduced dimensionality and can, therefore, be interpreted as a 2D topological insulator. Consequently, one-dimensional topological edge states appear at the edges of the multi-QW structure perpendicular to the growth direction of the QW as schematically illustrated in Fig. 7(b). They are spin polarized such that electrons of opposite spin counterpropagate at the sample edges. Such one-dimensional topological edge states have been detected in transport measurements in the similar case of HgTe/CdTe QW structures [11,22]. It is important to point out, that despite the fact that the underlying physical principles are the same in both cases, two totally different topological states are investigated in supercell calculations and in transport experiments, respectively. The transport of carriers in the 1D topological states is used to detect indications for the QSH phase in the QWs which has been characterized in Sec. III C by 2D topological interface states.

IV. SUMMARY AND CONCLUSIONS

We have presented a detailed *ab initio* analysis of α-Sn/CdTe(001) quantum wells depending on the thicknesses of both materials. The topological $\mathbb{Z}_2$ invariants of the respective strained bulk materials α-Sn and CdTe, have been computed. We found $\mathbb{Z}_2(\alpha\text{-Sn}) = 1$ and $\mathbb{Z}_2(\text{CdTe}) = 0$. This characterizes strained α-Sn as a 3D TI, whereas CdTe is a trivial insulator. We have shown that due to the different topologies of the two materials, a topological phase transition from a trivial insulating phase into the quantum spin Hall phase in the QW structures occurs for a critical α-Sn film thickness between $d_1 = 8.1$ nm and $d_1 = 9.4$ nm. In the nontrivial regime, the situation is similar to a series of interfaces between two half-spaces of α-Sn and CdTe. Consequently, the interfaces support 2D topological interface states, which we characterized in detail concerning their localization, linear **k** dispersion, and spin polarization.

Finally, we have pointed out, that the dimensionality of the QW structure determines the dimensionality of the occurring topological states, which is important to distinguish the 2D interface states from the 1D topological edge states, which have been found in transport measurements for finite QW structures. While supercell calculations with a 3D translational symmetry support the investigation of 2D interface states, most experiments use 2D Hall-bar structures made of QWs in the inverted regime. As these two-dimensional systems are 2D topological insulators, one-dimensional topological edge states must occur at their rim. Therefore, the theoretical results can only be interpreted as an indirect verification of the experimental transport findings and vice versa.

ACKNOWLEDGMENTS

We gratefully acknowledge financial support from the Austrian Fond zur Förderung der Wissenschaftlichen Forschung in the framework of SFB 25 Infrared Optical Nanostructures. L.M. thanks the Carl-Zeiss Foundation for a scholarship. The computations have been performed in part using the facilities of the John von Neumann Institute for Computing in Jülich.

[1] M. Z. Hasan and C. L. Kane, Rev. Mod. Phys. **82**, 3045 (2010).
[2] J. Moore, Nature (London) **464**, 194 (2010).
[3] X.-L. Qi and S.-C. Zhang, Rev. Mod. Phys. **83**, 1057 (2011).
[4] L. Müchler, H. Zhang, S. Chadov, Y. Binghai, F. Casper, J. Kübler, S. Zhang, and C. Felser, Angew. Chem., Int. Ed. **51**, 7221 (2012).
[5] Y. Ando, J. Phys. Soc. Jpn. **82**, 102001 (2013).

[6] J. E. Moore and L. Balents, Phys. Rev. B **75**, 121306 (2007).
[7] R. Roy, Phys. Rev. B **79**, 195322 (2009).
[8] L. Fu, C. L. Kane, and E. J. Mele, Phys. Rev. Lett. **98**, 106803 (2007).
[9] C. L. Kane and E. J. Mele, Phys. Rev. Lett. **95**, 146802 (2005).
[10] B. Andrei Bernevig, T. L. Hughes, and S.-C. Zhang, Science **314**, 1757 (2006).
[11] M. König, S. Wiedmann, C. Brüne, A. Roth, H. Buhmann, L. Molenkamp, X.-L. Qi, and S.-C. Zhang, Science **318**, 766 (2007).
[12] C. Liu, T. L. Hughes, X.-L. Qi, K. Wang, and S.-C. Zhang, Phys. Rev. Lett. **100**, 236601 (2008).
[13] J. Moore, Nat. Phys. **5**, 378 (2009).
[14] S. Murakami, N. Nagaosa, and S.-C. Zhang, Phys. Rev. Lett. **93**, 156804 (2004).
[15] I. Tsidilkowski, *Gapless Semiconductors—A New Class of Materials* (Akademie-Verlag, Berlin, 1988).
[16] J. R. Chelikowsky and M. L. Cohen, Phys. Rev. B **14**, 556 (1976).
[17] S. Küfner and F. Bechstedt, Phys. Rev. B **89**, 195312 (2014).
[18] L. Fu and C. L. Kane, Phys. Rev. B **76**, 045302 (2007).
[19] R. Yu, X. L. Qi, A. Bernevig, Z. Fang, and X. Dai, Phys. Rev. B **84**, 075119 (2011).
[20] J. Anversa, P. Piquini, A. Fazzio, and T. M. Schmidt, Phys. Rev. B **90**, 195311 (2014).
[21] S. Küfner and F. Bechstedt, Phys. Rev. B **91**, 035311 (2015).
[22] A. Roth, C. Brüne, H. Buhmann, L. W. Molenkamp, J. Maciejko, X.-L. Qi, and S.-C. Zhang, Science **325**, 294 (2009).
[23] P. Hohenberg and W. Kohn, Phys. Rev. **136**, B864 (1964).
[24] W. Kohn and L. J. Sham, Phys. Rev. **140**, A1133 (1965).
[25] G. Kresse and J. Furthmüller, Phys. Rev. B **54**, 11169 (1996).
[26] G. Kresse and J. Furthmüller, Comput. Mater. Sci. **6**, 15 (1996).
[27] D. M. Ceperley and B. J. Alder, Phys. Rev. Lett. **45**, 566 (1980).
[28] J. P. Perdew and A. Zunger, Phys. Rev. B **23**, 5048 (1981).
[29] D. Hobbs, G. Kresse, and J. Hafner, Phys. Rev. B **62**, 11556 (2000).
[30] P. E. Blöchl, Phys. Rev. B **50**, 17953 (1994).
[31] G. Kresse and D. Joubert, Phys. Rev. B **59**, 1758 (1999).
[32] H. J. Monkhorst and J. D. Pack, Phys. Rev. B **13**, 5188 (1976).
[33] R. Farrow, D. Robertson, G. Williams, A. Cullis, G. Jones, I. Young, and P. Dennis, J. Cryst. Growth **54**, 507 (1981).
[34] A. Thewlis and J. Davey, Nature (London) **174**, 1011 (1954).
[35] J. P. Perdew, J. A. Chevary, S. H. Vosko, K. A. Jackson, M. R. Pederson, D. J. Singh, and C. Fiolhais, Phys. Rev. B **46**, 6671 (1992).
[36] A. R. West, *Basic Solid State Chemistry* (Wiley, New York, 1988).
[37] W. Martienssen and H. Warlimont, *Springer Handbook of Condensed Matter and Materials Data*, Bd. 1 (Springer, New York, 2005).
[38] W. G. Aulbur, L. Jönsson, and J. W. Wilkins, in *Solid State Physics*, Solid State Physics Vol. 54, edited by H. Ehrenreich and F. Saepen (Academic, New York, 1999), pp. 1–218.
[39] S. Küfner, J. Furthmüller, L. Matthes, M. Fitzner, and F. Bechstedt, Phys. Rev. B **87**, 235307 (2013).
[40] J. Heyd, G. E. Scuseria, and M. Ernzerhof, J. Chem. Phys. **118**, 8207 (2003).
[41] F. Tran and P. Blaha, Phys. Rev. Lett. **102**, 226401 (2009).
[42] J. D. Talman and W. F. Shadwick, Phys. Rev. A **14**, 36 (1976).
[43] Y.-S. Kim, M. Marsman, G. Kresse, F. Tran, and P. Blaha, Phys. Rev. B **82**, 205212 (2010).
[44] Y.-S. Kim, K. Hummer, and G. Kresse, Phys. Rev. B **80**, 035203 (2009).
[45] F. Bechstedt, *Principles of Surface Physics* (Springer-Verlag, Berlin, 2003).
[46] J. N. Schulman and Y.-C. Chang, Phys. Rev. B **33**, 2594 (1986).
[47] O. Madelung, *Semiconductors: Group IV Elements and III-V Compounds* (Springer-Verlag, Berlin, 1991).
[48] L. Fu and C. L. Kane, Phys. Rev. B **74**, 195312 (2006).
[49] A. A. Soluyanov and D. Vanderbilt, Phys. Rev. B **83**, 235401 (2011).
[50] E. Prodan, Phys. Rev. B **83**, 235115 (2011).
[51] L. Winterfeld, L. A. Agapito, J. Li, N. Kioussis, P. Blaha, and Y. P. Chen, Phys. Rev. B **87**, 075143 (2013).
[52] S. Küfner, M. Fitzner, and F. Bechstedt, Phys. Rev. B **90**, 125312 (2014).
[53] H. Lüth, *Solid Surfaces, Interfaces and Thin Films* (Springer, Berlin, 2001).
[54] J. Tersoff, Phys. Rev. B **30**, 4874 (1984).
[55] A. Schleife, F. Fuchs, C. Rödl, J. Furthmüller, and F. Bechstedt, Appl. Phys. Lett. **94**, 012104 (2009).
[56] H. Ibach and H. Lüth, *Festkörperphysik: Einführung in die Grundlagen* (Springer, Berlin, 1995).
[57] B. Höffling, A. Schleife, C. Rödl, and F. Bechstedt, Phys. Rev. B **85**, 035305 (2012).
[58] B. Höffling, A. Schleife, F. Fuchs, C. Rödl, and F. Bechstedt, Appl. Phys. Lett. **97**, 032116 (2010).
[59] A. Barfuss, L. Dudy, M. R. Scholz, H. Roth, P. Höpfner, C. Blumenstein, G. Landolt, J. H. Dil, N. C. Plumb, M. Radovic, A. Bostwick, E. Rotenberg, A. Fleszar, G. Bihlmayer, D. Wortmann, G. Li, W. Hanke, R. Claessen, and J. Schäfer, Phys. Rev. Lett. **111**, 157205 (2013).
[60] Y. Ohtsubo, P. Le Fèvre, F. Bertran, and A. Taleb-Ibrahimi, Phys. Rev. Lett. **111**, 216401 (2013).